Chapter 7

Outlook and possible future directions

Since time immemorial, mathematicians and artists alike fancied helices and spirals. Prominent in ancient ornaments, spiral shape most famously showed up in Watson and Crick' double helical model of DNA. Helical shapes of fibers, bands, and bundles is generally one of the Nature's greatest schemes for self-assembly, growth, and structural integrity presented in: aromatics [77] (see also News and Views on this subject in [78]), tendrils of plants [79], proteins, DNA [80], the heart, etc. How these helical structures self-assemble is often a mystery: sometimes, like in proteins, it is possible to show that the transformation is entropically driven [81], but oftentimes it is not known how these helices form [82]. As Martin Kemp famously observed in his elegant treatise on "spirals of life," the helical living designs are generally well known for their static features, rather than their active function [63]. Of course, airplane propeller or bacterium flagella represent rotating spiral designs, but in both cases the spiral itself is still passive.

That is why we were much excited to learn that while all the fibers in the myocardium were helically organized for structural integrity, the active muscle fibers in the heart appear to have a sort of double helical organization as well, as it was recently observed by the modern sophisticated imaging technique – version of MRI called DTMRI [23]. The apparently dominant helical organization of fibers in the heart raises a more serious question: Is it possible that spiral organization of the active myofibrils may also shed light on the complex dynamics of the heart?

We started thinking that these spiral structures might hold the key to understand the wonderfully efficient function of the heart. Indeed, the muscle band consists of a group of parallel muscle fibers, each of which cannot contract much over 15%, yet the volume exchange ratios, ejection fractions, in the ventricles can exceed 60%. Is it possible to gain an insight into these paradox by invoking the spiral geometry of the muscle band?

H.T. Crane once wrote on the general problems of biological growth. He pointed out, that while the process in the whole can be too complex for us to produce an equation describing it, we can

understand it if we know "the principles involved and something of the order of their importance"[62]. In studying the development of the heart I followed this road-map.

The most efficient way to approach these problem is by using computational modeling.

We constructed an efficient computational model in chapter 2 by assuming that the myofibrils are arranged in the heart muscle is a single band that starts from the pulmonary aorta, hugs the right ventricle, winds down to the apex, as the descending segment, and then spirals up to the aortic valve as the ascending segment. We assumed that this band reacts to the local strain created by excitation of the muscle cells as an elastic body, while the rest of the myocardium is a passive material that does not create any strain and just bounds the volume. This allowed us to resort to very advanced computational techniques used in other well developed engineering fields, and even use a commercially available finite element package – ABAQUS [74]. Simplistically, this program solves elastic equilibrium equations for each small cuboid, and then puts together the evolution of the whole structure by continuity.

The advantage of computational modeling is that once the computational model is set up it allows for easy testing of a wide variety of conditions. We can vary the fiber angles, width, thickness, and ventricle dimensions. The band can shorten as a whole, or parts of it can contract independently of each other. This allows us to create complicated contraction schemes inside the band.

The simplest dynamic scheme is to excite all the nodes at the same time and have the elements contracting in sync, making a uniform contraction. More interestingly, we are able to mimic the action of the Purkinje network by considering an excitation/relaxation wave traveling along our band starting at the apex.

The first success of our model is its ability to effortlessly resolve the above mentioned paradox and to reproduce the large ejection fraction, despite the small muscle strain. It came as a pleasant surprise that our model easily matches not only the physiological maximum ejection fraction, but also the left ventricular volume evolution with time as was shown in chapter 2.

In chapter 3 we use this approach of focusing on dominant structures in the heart to investigate the causes of the forces that play an integral role in the self-assembly of the adult four chamber heart from the embryonic tube heart. We showed that the helical form of the fibers surrounding the heart tube in combination with a spatial excitation wave is able to produce the twisting forces necessary for the initiation of self-assembly.

We then turned, in chapter 4, to a much more sensitive property of the heart, namely the timing relationship between twist and ejection fraction, which is considered a potentially powerful diagnostic tool of ventricular health. While comparing the model results to actual physiological data, we were gratified to find that we can match the double looped response observed in nature, and that this is possible only with an excitation that approximated the physiological scheme.

In chapter 5 we used our model to consider pathological behaviors of the heart. Indeed, because

of the relatively simple nature of the double helical model we are able to test different types of damage separately, and to discern the causes of pathological behavior. As we have shown, for dilated cardiomyopathy the change in fiber angle is much more critical than the change in gross geometry of the left ventricular chamber. Additionally, we were able to match experimental results for the relationship between twist and ejection fraction seen in cases of dilated cardiomyopathy, giving more credence to the computational model.

Finally, in chapter 6 we demonstrated that the double helical muscle band used as an engine inside a collagen shell can produce physiologically high pressures. This filled-out model will be the springboard into further research. Indeed, to model both the pressure generation and volume ejection of the ventricles we need to match the highly nonlinear behavior of the heart tissue. It will be necessary to model the endocardium membrane that is very resistent to stretching, as well as the ability of the collagen matrix to shear with the movement of the muscle fibers, while increasing the width of the walls.

What have we learned from this model? In general the greatest benefits of modeling is to gain insight into the dominant structures and processes. In our case, the model was initially proposed by Torrent-Guasp and supported by modern imaging techniques, such as DTMRI, but is still not uniformly accepted by researchers in the field. Our modeling results indicate that helical arrangement of the muscle in the heart does provide a natural and simple explanation of heart pumping. This insight predicts that the heart cells grown around a scaffold in recent breakthrough research by a Minnesota group will need an additional input to provide them with proper organization, in order to transform their wonderfully achieved beating into efficient pumping. We hope our results will be valuable in this endeavor.

The imagination of great artist allowed M.C. Escher to portray the human face as an elegantly bent paper stripe (Rind 1955). When we look at the image we unmistakably see the human head and face, and even quite expressive face. Is this model physiologically correct, does it involve all the physiologically relevant details? No, it does not. But it does capture something important – in fact, something most essential for the artist. We hope that, similarly, our model, however simplified, does capture something most essential. Definitely, it can serve as a starting point for further research, as it helps asking useful questions to be addressed by MRI and other studies.

Appendix A

Additional Analytical Calculations

A.1 Inherent limit on pumping efficiency of structures with non-helical fibers

Let us first consider a tubular and a parabolic pumping chamber with non-helical fibers. We impose the same boundary and material conditions as were described in section 2.2. We expect the biggest ejection fraction to be produced by the biggest possible fiber contraction of 15%.

A tube volume is given by $V = \pi r^2 L$, where r is the radius and L is length. For a parabolic chamber the volume is given by $V = (1/2)\pi r_{max}^2 L$, where L is the height of the parabola, and r_{max} is the radius at height L. For both of these, if the fibers are arranged circumferentially the circumference, and thus the radius will decrease by 15%, i.e., $r = 0.85 r_0$.

Using equation 2.8 the ejection fraction would be about 28%. However, in the tube model the ejection fraction would actually be lower, because the two ends of the tube are fixed, so that the fibers close to the ends cannot contract and will simply exhibit stress in response to excitation. This is also the case for the basal region of the parabolic chamber.

If the fibers are arranged longitudinally then the in the tube model there will be no pumping at all because the length is restricted from shortening by the boundary conditions. For the parabolic chamber the length will be reduced by 15%, and thus the ejection fraction would also be 15%.

Appendix B

Analytical estimate of energy efficiency of twist vs. contraction pumps

B.1 Introduction

There is heuristic evidence that twisting action is very important in pumping mechanisms [64]. Here we present a range of analytical models called on to illustrate one of the reasons behind nature's propensity of taking advantage of the effect of twisting.

B.2 Pumping from a Cylindrical shell

We create analytical models for tube-pumping mechanisms. Such pumps are used extensively, for example inside the body to increase the flow through the vasculature. We will use the notion of the ejection fraction to evaluate the output of our simple pumps. The ejection fraction, EF, is given by the change of volume normalized by the initial volume:

$$EF = \frac{V_0 - V}{V_0} = 1 - \frac{V}{V_0}. \tag{B.1}$$

Let us considering two different systems, one that has the tube contracting radially while the other is twisted.

B.2.1 Radial shortening of the tube

Let us first consider squeezing the tube radially, as seen in figure B.1. In this case we have circular wires, with radius r_{wire} arranged around a cylinder of constant length $L = L_0$, and initial radius of

r_0, and the initial fiber length of $D_0 = 2\pi r_0$. The volume of the cylinder is simply given by:

$$V = L \cdot \pi r^2. \tag{B.2}$$

In this model the wires will shorten around the tube by a factor of ε, meaning that the fiber length is $D = (1-\varepsilon)D_0 = 2(1-\varepsilon)\pi r_0 = 2\pi r$. And thus $r = (1-\varepsilon)r_0$. Since the length of the cylinder is constant we use equation B.1 and get the ejection fraction to be:

$$EF = 1 - \frac{r^2}{r_0^2} = 1 - \frac{(1-\varepsilon)^2 r_0^2}{r_0^2} = 2\varepsilon - \varepsilon^2. \tag{B.3}$$

The difficulty with such a pump is that a device which uses shortening of wires to pump would be energetically very expansive, which is easy to prove to oneself by simply bending a wire and then trying to shorten it – it takes a great deal more effort to shorten something than it does to bend it. However, there are at least two simple ways to create radial shortening in the tube while bending the wires. In the first case, the wire slides into a spiral form, as seen in figure B.2(a). In this case the model would become invalid once the radius of the tube becomes comparable to the radius of the wire. A second simple device is akin to a snake eating its own tail, where we create a slit in one half of the wire that the second half can slide into (figure B.2(b)). In this case the minimum circumference can be only half of the wire length, $\varepsilon_{max} = 0.5$, but that would mean an ejection fraction of $EF = 75\%$, which is sufficient for most applications. Thus both of these models are considered.

The work used to achieve the volume change for both of these models is the bending energy of the wires. Assuming that the fibers are initially stress free, and that linear elasticity applies, the

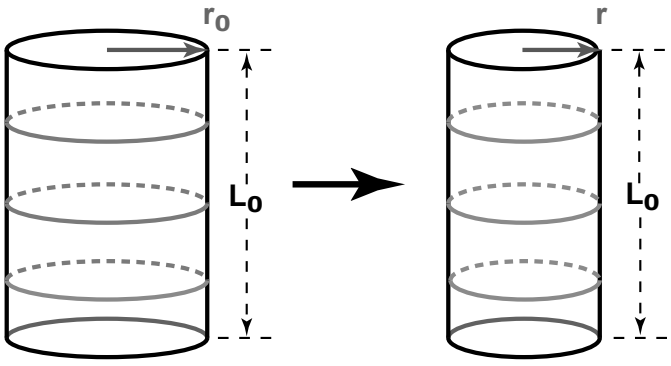

Figure B.1: A schematic of radially squeezed tube, with a few wires drawn.

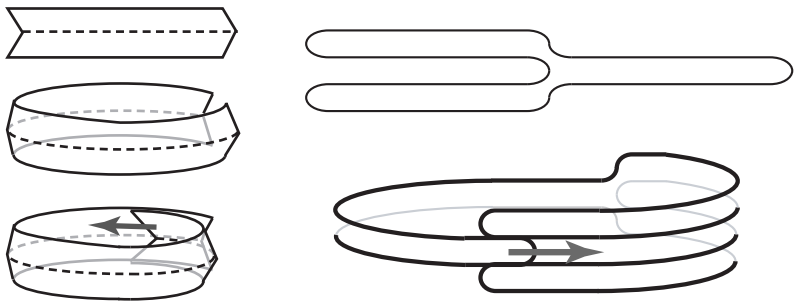

(a) Spiral wire (b) Snake wire

Figure B.2: Two different ways to create radial shortening through bending of the wires.

energy to reduce the radius of the tube can be calculated by:

$$E = \frac{1}{2}kD\left(\frac{1}{R} - \frac{1}{R_0}\right)^2, \tag{B.4}$$

$$k = \frac{1}{4}E_Y \pi r_{wire}^4, \tag{B.5}$$

where E_Y is the Young's modulus of elasticity for the wires, R and R_0 are the current and initial radii of curvature, respectively. For radial wires the radius of curvature is simply the current radius of the tube. For the purpose of these calculations we will assume that the average wire radius is the same in both of the cases that we proposed above, which means that both cases require the same amount of work to shorten the circumference of the tube.

$$E = \frac{1}{2}kD_0\left(\frac{1}{r} - \frac{1}{r_0}\right)^2 = \frac{kD_0}{2r_0^2}\left(\frac{r_0}{r} - 1\right)^2. \tag{B.6}$$

As mentioned before, in these calculations we assume that $r \gg r_{wire}$ and we will assume so for all of these analytical models. Another scaling assumption that we need to make is that the distance between fibers is much greater than the diameter of the fibers. For now let us assume that there are n wires. By manipulating equation B.3, we can find that:

$$\frac{r_0}{r} = \frac{1}{\sqrt{1-EF}} \quad \Rightarrow \tag{B.7}$$

$$\Rightarrow \quad \left[\frac{r_0}{r} - 1\right]^2 = \left[\frac{1-\sqrt{1-EF}}{\sqrt{1-EF}}\right]^2 = \frac{\left(1-\sqrt{1-EF}\right)^2}{1-EF}. \tag{B.8}$$

Applying this to equation B.6 we can find the total work performed as a function of the ejection

fraction achieved:

$$E = \frac{nkD_0}{2r_0^2}\frac{\left(1-\sqrt{1-EF}\right)^2}{1-EF}. \tag{B.9}$$

We can write this work in a dimensionless form:

$$\widetilde{E} = \frac{E}{E_Y \pi r_{wire}^2 r_0} = \frac{nr_{wire}^2 D_0}{8r_0^3}\frac{\left(1-\sqrt{1-EF}\right)^2}{1-EF}. \tag{B.10}$$

A plot of the work required for the pumping as a function of the ejection fraction is shown in figure B.3. Note that the plot does not extend beyond ninety percent ejection fraction, because the radius of the tube becomes comparable to the radius of the wires at that point and the model breaks down, and thus the work approaches infinity for an ejection fraction of one.

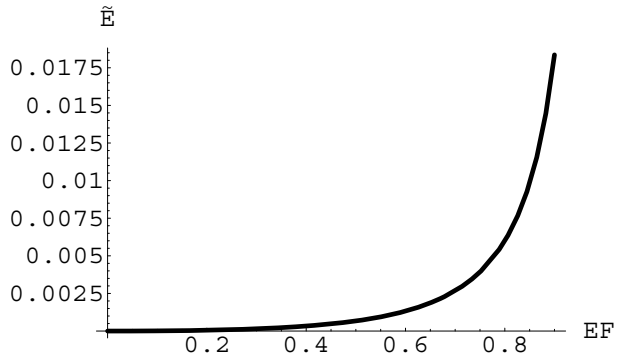

Figure B.3: The plot of work required vs. the ejection fraction achieved for radial contraction in a tube, n=5.

B.2.2 Twisting of the tube

Now Let us consider a cylinder made up of non-extendable longitudinal or helical wires. Again the wire radius is r_{wire} and its constant length is $D = D_0$. The cylinder has a constant radius of $r = r_0$ and an initial length of L_0. For this model the top edge of the cylinder is held, while the bottom is rotated by an angle α (figure B.4). In this case the assumption that the distance between the fibers is much larger than the diameter of the fibers is very important. If this assumption is valid, the work put into this transformation, is the bending energy. However, if this assumption is not true and the fibers are close enough to interact with one another during the transformation the bending energy will no longer be a dominating factor. For this analytical problem we will also assume that there will be no buckling.

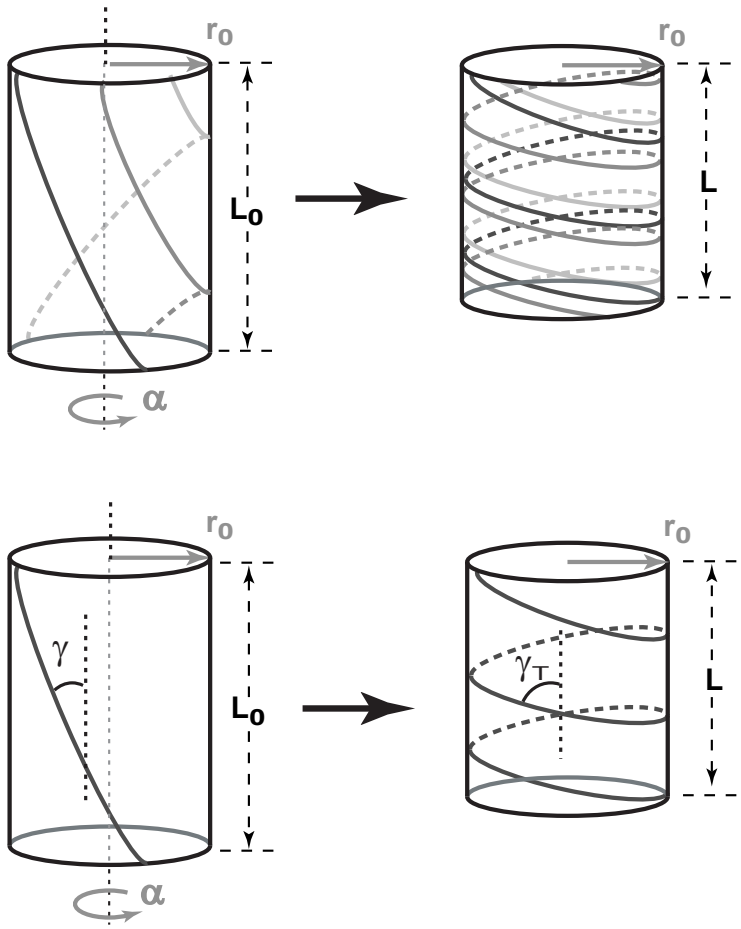

Figure B.4: Twisting of helically arranged fibers. The top series shows the tube with several wires. The bottom shows only one wire, and labels the relevant twist angles.

The length of the tube can be written in terms of the turn angle:

$$L = \sqrt{D^2 - \alpha^2 r^2}. \tag{B.11}$$

Let us assume that initially the fibers are at an angle γ to the vertical (figure B.4). If this angle is $\gamma = 0$ then the length of the tube is the same as the fiber length, $L_0 = D$. Substituting these into the equation B.2 and B.1 we have:

$$EF = 1 - \frac{L}{L_0} = 1 - \frac{\sqrt{D^2 - \alpha^2 r^2}}{D} = 1 - \sqrt{1 - \left(\frac{\alpha r}{D}\right)^2}. \tag{B.12}$$

However, if initially the unstressed fibers are helical and $\gamma \neq 0$, the starting twist needs to be taken into account. It is important to note that $0 \leq \gamma \leq \pi/2$. For volume calculations this can be interpreted as though we first rotated the bottom edge by an angle β, which is given by the known

twist angle,γ:

$$\beta = \frac{D \sin\gamma}{r}. \tag{B.13}$$

Now we can use equations B.11,B.2 and B.1 to write the ejection fraction as a function of both the initial turn angle and the additional turn angle:

$$EF = 1 - \frac{L}{L_0} = 1 - \sqrt{\frac{D^2 - (\alpha+\beta)^2 r^2}{D^2 - \beta^2 r^2}} = 1 - \sqrt{\frac{D^2 - (\alpha r + D\sin\gamma)^2}{D^2\left(1-\sin^2\gamma\right)}}. \tag{B.14}$$

After the transformation the total angle that the fiber makes to the vertical is going to be:

$$\sin\gamma_t = \frac{r\left(\alpha+\beta\right)}{D} = \frac{\alpha r}{D} + \sin\gamma. \tag{B.15}$$

The total γ_t also has to be between zero and $\pi/2$, which puts a constraints on α.

$$-\frac{D\left(\sin\gamma\right)}{r} \leq \alpha \leq \frac{D\left(1-\sin\gamma\right)}{r}. \tag{B.16}$$

However, if $\alpha < 0$, there would be no pumping. The upper limit on α would actually be constrained by the radius of the wire. Indeed the distance between the wires has to be greater than the diameter of the wire (figure B.5). This constrains the total twist angle to:

$$x > 2r_{wire} \quad \Rightarrow \quad \cos^2\gamma_t > \frac{nr_{wire}}{\pi r} \quad \Rightarrow \quad \sin\gamma_t < \sqrt{1-\left(\frac{nr_{wire}}{\pi r}\right)^2} \tag{B.17}$$

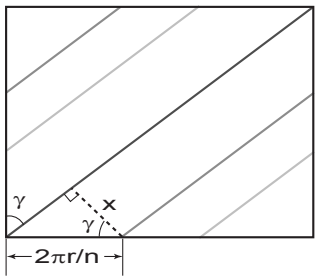

Figure B.5: The cylinder laid out flat, showing the twist angle and the distance between the wires.

That means that the limit on maximal turn angle that we can induce is:

$$\alpha < \frac{D}{r}\left[\sqrt{1-\left(\frac{nr_{wire}}{\pi r}\right)^2} - \sin\gamma\right], \tag{B.18}$$

which puts a constraint on the ejection fraction that can be reached with this device:

$$EF < 1 - \frac{1}{\cos\gamma}\left(\frac{nr_{wire}}{\pi r}\right). \tag{B.19}$$

Figure B.6 shows the relationship between the initial twist angle, γ, and the maximum ejection fraction that can be achieved.

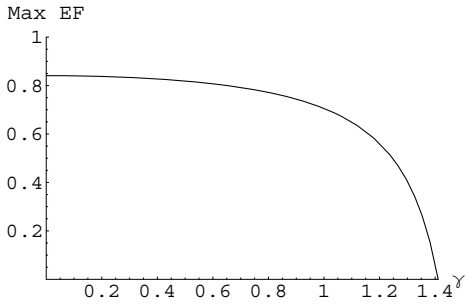

Figure B.6: The maximum ejection fraction possible with the twist method as a function of γ. Constants: $n = 5$,$D = 2\pi r$,$r_{wire} = 0.1r$.

To calculate the work used to make these transformations we can calculate the energy of bending (formula B.4) for one wire undergoing this twisting. Substituting the relationship of equation B.13 into equation C.17 from the appendix C.3 we have the expression for the radii of curvature in terms of the turn angles:

$$R_0 = \frac{D^2}{\beta^2 r} = \frac{r}{\sin^2\gamma}\ , \qquad R = \frac{D^2}{(\alpha+\beta)^2 r} = \frac{D^2}{\left(\alpha + \frac{D\sin\gamma}{r}\right)^2 r}. \tag{B.20}$$

Plugging these into equation B.4, for one wire the work to bend it will be:

$$E = \frac{k_2}{2}\frac{r^2}{D^3}\alpha^2(\alpha+2\beta)^2 = \frac{k_2}{2}\frac{r^2}{D^3}\alpha^2\left(\alpha + 2\frac{D\sin\gamma}{r}\right)^2. \tag{B.21}$$

This can be used to write the relationship between work and ejection fraction. Assuming we have n wires the work will be:

$$E = \frac{k_2 n}{2}\frac{D}{r^2}\left[1 - \left(\frac{\beta r}{D}\right)^2\right]^2 \left[2EF - EF^2\right]^2 = \tag{B.22}$$

$$= \frac{k_2 n}{2}\frac{D}{r^2}\cos^4\gamma\left[2EF - EF^2\right]^2. \tag{B.23}$$

If we write it in the same dimensionless form as for the previous case we have:

$$\widetilde{E} = \frac{E}{E_Y \pi r_{wire}^2 r_0} = \frac{nD_0}{8r_0}\left(\frac{r_{wire}}{r}\right)^2\left[1-\left(\frac{\beta r}{D}\right)^2\right]^2\left[2EF - EF^2\right]^2 = \tag{B.24}$$

$$= \widetilde{E} = \frac{nD_0}{8r_0}\left(\frac{r_{wire}}{r}\right)^2 \cos^4\gamma\left[2EF - EF^2\right]^2. \tag{B.25}$$

It is important to note that unlike the radial shortening case the initial length of the wire is independent of the initial radius of the tube for the twisting model. If the length of the fiber is the same as the initial circumference of the cylinder, then the ejection fraction and work for the twist case can be written as:

$$EF = 1 - \frac{\sqrt{1-\left(\frac{\alpha}{2\pi}+\sin\gamma\right)^2}}{\cos\gamma} \tag{B.26}$$

$$\widetilde{E} = \frac{n\pi}{4}\left(\frac{r_{wire}}{r}\right)^2 \cos^4\gamma\left[2EF - EF^2\right]^2. \tag{B.27}$$

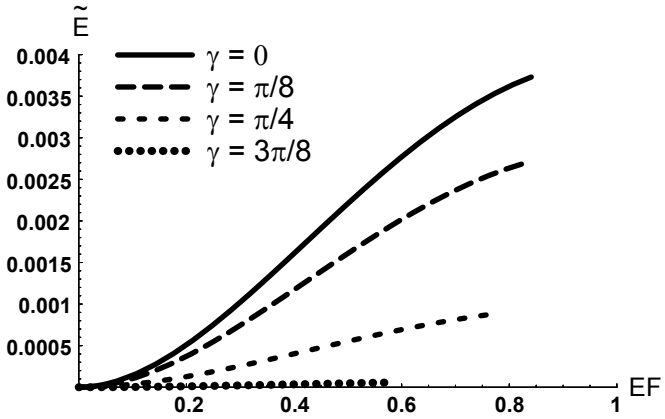

Figure B.7: The plot of work required vs. the ejection fraction achieved for twisting of the bottom of the tube. There are multiple curves for several initial twist angles, γ values, $n = 5$,$D = 2\pi r$,$r_{wire} = 0.1r$

.

This dimensionless work is plotted for several values of the initial twist angle in figure B.7, with the same values for the constants as in the case of the radial shortening. Each curve stops at the maximum ejection fraction that can be achieved with the starting twist angle. Note that the most efficient way to get a specific ejection fraction is to pick the maximum initial angle at which it is possible to get that ejection fraction. Indeed if we assume that the most efficient path to each specific ejection fraction is taken we can rewrite the work relationship as:

$$\widetilde{E} = \frac{nD_0}{8r_0}\left(\frac{r_{wire}}{r}\right)^2\left(\frac{nr_{wire}}{\pi r}\right)^4 \frac{\left[2EF_{max} - EF_{max}^2\right]^2}{\left(1-EF_{max}\right)^4}. \tag{B.28}$$

Note that $r_{wire}/r_0 \ll 1$, so even if the length of the wire is increased this device will remain more efficient than the one that has radial shortening.

B.2.3 Pumping against inner pressure

Working with linear elasticity it is relatively easy to consider the work required to overcome the pressure inside the tube. Indeed for a tube that has inner pressure, P_{in}, and the pressure outside is P_{out}, we can use the volume calculations for both models to show:

$$\begin{aligned} E_{pressure} &= (P_{out} - P_{in})\Delta V = (P_{out} - P_{in})(V - V_0) = \\ &= (P_{out} - P_{in})V_0 \frac{V - V_0}{V_0} = -EF(P_{out} - P_{in})V_0 \end{aligned} \tag{B.29}$$

This energy is not dependent on the way we achieve the ejection fraction, and will be the same for all the devices considered here, and can be added to the work calculated in the previous sections.

B.2.4 Comparing the two different methods of pumping

To see how the different methods of pumping compare we plot the dimensionless energies on the same plot, cutting the ejection fraction at 75%, since higher ejection fractions are not of interest here (figure B.8). At first glance it seems that for some ejection fractions the radial contraction device is more efficient than the twisting device. However, if for each ejection fraction the γ is chosen such that the work is most efficient to reach that ejection fraction, the results clearly show that the twisting is a better choice (figure B.9). Another way to look at it is to show the work required for the two different models when the maximal desired ejection fraction is known. Such a plot for three different ejection fractions is shown in figure B.10.

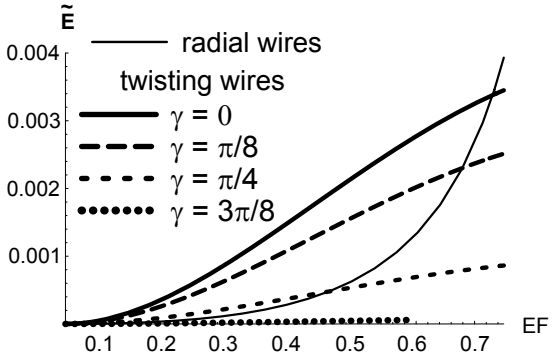

Figure B.8: The plot of work required vs. the ejection fraction achieved for both the twisting of the bottom of the tube and radial shortening of wires. There are multiple curves for several initial twist angles, γ values. All the constants are the same for both cases: $n = 5$,$D = 2\pi r$,$r_{wire} = 0.1r$.

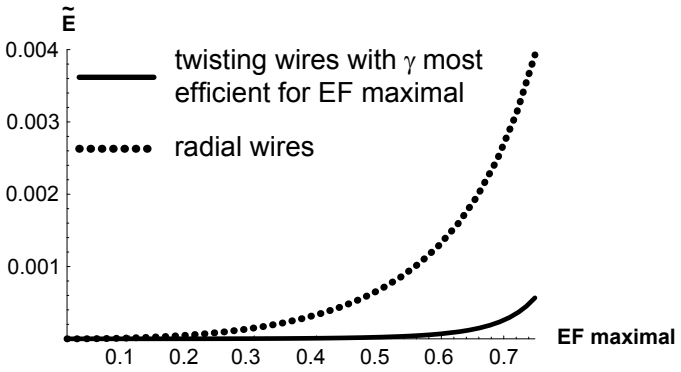

Figure B.9: The plot of work required vs. the maximal ejection fraction achieved for both the radial shortening of wires and the most efficient twisting of the bottom of the tube. All the constants are the same for both cases: $n = 5$,$D = 2\pi r$,$r_{wire} = 0.1r$.

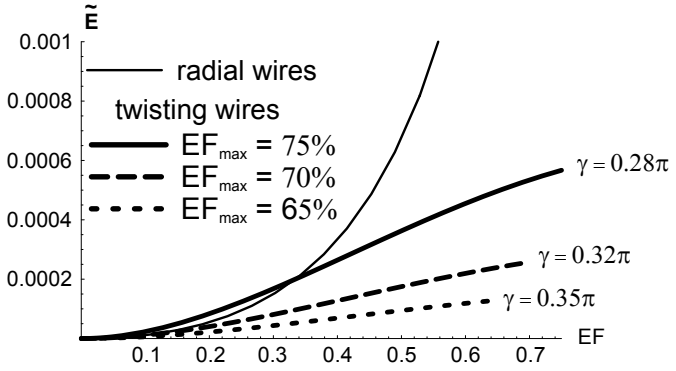

Figure B.10: The plot of work required vs. the ejection fraction achieved for both the twisting of the bottom of the tube and radial shortening of wires. There are multiple curves for several different maximal ejection fractions. All the constants are the same for both cases: $n = 5$,$D = 2\pi r$,$r_{wire} = 0.1r$.

B.3 Pumping from a half ellipsoid shell

Now let us consider pumping from a half ellipsoid shell. A biological example of such a pump would be the four chamber heart. We could potentially use the same method we did when describing the cylindrical pumps. This would not be very hard for radially contracting wires, but for helical wires it would require some very complicated mathematical expressions to describe the helix and calculate the radius of curvature in ellipsoid coordinates. Additionally, if later at some point we wanted to change the geometry of our chamber we would have to perform all the calculations again from scratch. So instead we will formulate an approximation method that will work quite well for a range of geometries.

Let us approximate the ellipsoid shell by a series of cylinders with each having a height dz. Each cylinder will have a radius of $r(z)$, which will determine the shape of our chamber. For example the

elliptical shell we will consider here will have

$$r = C \sinh \xi \sin \theta, \tag{B.30}$$

$$z = C \cosh \xi \cos \theta, \tag{B.31}$$

where C and ξ are constants, and θ is the parametric variable for a heart model varying $\frac{3\pi}{10} \leq \theta \leq \pi$.

We will now set up a formulation for calculating the ejection fraction of our convex shell pump. The volume of the shell will be the sum of the volumes of the cylinders that it is made up of. For the approximation to be accurate let us assume that $dz \to 0$, then instead of a sum we can write the volume in integral form. The initial volume would be given by:

$$V_0 = \pi \int_{z_0}^{z_{max}} [r(z)]^2 \, dz \tag{B.32}$$

where z_0 and z_{max} are the initial and final height of the shell, respectively. How the volume changes will depend on how each cylinder in the stack will deform.

B.3.1 Radial Contraction in a Shell

If we have radial wires about an axisymmetric shell of shape $r(z)$ each contracting the same way as described in section B.2.1. Thus the radius changes $r_f(z) = (1-\varepsilon)r(z)$ (note that $r(z)$ here is the initial radius). Then the volume is given by:

$$V = \pi \int_{z_0}^{z_{max}} [r_f(z)]^2 \, dz = \pi(1-\varepsilon)^2 \int_{z_0}^{z_{max}} \left[r_(z)\right]^2 dz = (1-\varepsilon)^2 V_0, \tag{B.33}$$

which means that the ejection fraction is the same as in equation B.3.

$$EF = 1 - (1-\varepsilon)^2 = 2\varepsilon - \varepsilon^2. \tag{B.34}$$

The energy for each wire is given by:

$$E_{one} = \frac{kD_0(z)}{2r(z)^2} \left(\frac{r(z)}{r_f(z)} - 1 \right)^2 = \frac{k\pi}{r(z)} \left(\frac{\varepsilon}{1-\varepsilon} \right)^2. \tag{B.35}$$

Thus for multiple wires the energy would become:

$$E = k\pi \left(\frac{\varepsilon}{1-\varepsilon} \right)^2 \sum_{i=1}^{n} \frac{1}{r(z_i)}, \tag{B.36}$$

where, i is the number of the wire. Since there is no single initial radius we will normalize this differently from the tube case:

$$\widetilde{E} = \frac{E}{E_Y \pi r_{wire}^3} = \frac{r_{wire}\pi}{4}\left(\frac{\varepsilon}{1-\varepsilon}\right)^2 \sum_{i=1}^{n} \frac{1}{r(z_i)}. \tag{B.37}$$

B.3.2 Twisting of a Shell

When each disk is twisted it will respond in the same way as the cylinder described in section B.2.2. That means that we assume that the radius does not change while the height becomes dz'. The new height will be given by:

$$dz' = \frac{L}{L_0} dz. \tag{B.38}$$

And the new volume will become:

$$V = \pi \int_{z_0}^{z_{max}} [r(z)]^2 \left(\frac{dz'}{dz}\right) dz = \pi \int_{z_0}^{z_{max}} [r(z)]^2 \left(\frac{L}{L_0}\right) dz. \tag{B.39}$$

The ratio of the initial and final length can be taken from section B.2.2. The energy can be calculated in the same way, since we know that the total work that needs to be done is the sum of the work used to turn each disk we will have dE rewritten from equation B.4:

$$dE = \frac{k_2}{2} [r(z)]^2 \left(\frac{d\alpha}{dD}\right)^2 \left[\frac{d\alpha}{dD} + 2\frac{\sin\gamma}{r(z)}\right]^2 dD. \tag{B.40}$$

However, now we need to determine the boundary conditions on each of the disks so that we can apply the equations we derived for the cylinder. We specify that the bottom of the shell is rotated by α, while the top is held immobile. This means that a disk somewhere in the middle will have one rotation at the top and a bigger rotation on the bottom. However, from a solid mechanics point of view if we are rotating the whole disk as a whole, it will not experience any deformations. This means that the only rotation that will impact the shape of the disk is the difference in the rotation of the top and bottom. To use our previous formulas we can look at each disk relative to its top (now immobile) with the bottom rotating by $d\alpha$. There are multiple ways to specify $d\alpha$ as a function of z, that we will describe a little later. The other quantity that is different for each disk is the length of the wire in each disk. Obviously, this will depend on the initial fiber angle, but it will also be a function of the shape of the shell under study:

$$dD = \frac{dz}{cos\gamma}, \tag{B.41}$$

where dD is the length of fiber at each disk, as previously γ and dz is the initial fiber angle and the height of each disk, respectively. For this study we will specify that γ will not depend on z.

This means that if we are considering an ellipsoid shell, the angle γ is the angle that is made by the projection of the tangent to the fiber on the $z-\theta$ plane and the z vector. Notice, that for each disk both $d\alpha$ and dD will be small quantities, thus we will rearrange the equations for the ratio of the lengths to combine these:

$$\frac{L}{L_0} = \frac{1}{\cos\gamma}\sqrt{1-\left[\left(\frac{d\alpha}{dD}\right)r(z)+\sin\gamma\right]^2}. \tag{B.42}$$

And the total energy can be written as:

$$E = \frac{k_2}{2\cos\gamma}\int_{z_0}^{z_{max}}\left(\frac{d\alpha}{dD}\right)^2\left[\frac{d\alpha}{dD}r(z)+2\sin\gamma\right]^2 dz. \tag{B.43}$$

Now let us consider the different possibilities for specifying $d\alpha$ on the disks.

The simplest rule would be to enforce that the rotations varies linearly with z, i.e., $d\alpha = \frac{\alpha}{L_0}dz$. This has the benefit of being simple, with the "small" ratio becoming:

$$\frac{d\alpha}{dD} = \frac{\alpha\cos\gamma}{L_0}. \tag{B.44}$$

And the length ratio becomes:

$$\frac{L}{L_0} = \frac{1}{\cos\gamma}\sqrt{1-\left[\left(\frac{\alpha\cos\gamma}{L_0}\right)r(z)+\sin\gamma\right]^2}. \tag{B.45}$$

Substituting this into equation B.39 to find the final volume of the shell we have:

$$V = \pi\int_{z_0}^{z_{max}}\frac{[r(z)]^2}{\cos\gamma}\sqrt{1-\left[\left(\frac{\alpha\cos\gamma}{L_0}\right)r(z)+\sin\gamma\right]^2}\,dz. \tag{B.46}$$

The ejection fraction is simply given by equation B.1. The energy can be calculated to be:

$$E = \frac{k_2\cos\gamma}{2}\left(\frac{\alpha}{L_0}\right)^2\int_{z_0}^{z_{max}}\left[\frac{\alpha\cos\gamma}{L_0}r(z)+2\sin\gamma\right]^2 dz. \tag{B.47}$$

We need to normalize this expression differently from what was done in the cylinder case since the radius varies with z. This will not matter since we will only be comparing the energies of the shell being twisted and radially contracted. So we will have:

$$\widetilde{E} = \frac{E}{E_Y\pi r_{wire}^3} = \frac{r_{wire}\cos\gamma}{8}\left(\frac{\alpha}{L_0}\right)^2\int_{z_0}^{z_{max}}\left[\frac{\alpha\cos\gamma}{L_0}r(z)+2\sin\gamma\right]^2 dz. \tag{B.48}$$

While considerably more complicated these expressions have the same nature as in the case of a cylinder and predictably the same result.

B.4 Conclusion

The simple analytical problems presented here showcase of the importance of twist in pumping devices. These are of course grossly simplified, ignoring effects like buckling. However the results help us develop an instinctive understanding of the importance of twisting in biological pumps.

Appendix C

Additional Methods

C.1 Geometrical parameters in formulating the Double helical heart: healthy and diseased

In this model we assume that the double helical band to approximate the myocardium fiber architecture. While detailed description of how these equations are formulated will be published elsewhere, we give a brief overview here. As a first step we describe the changing orientation of the fibers by specifying the long-axis coordinate, z_{cent}, as a function of polar coordinate θ for the centerline of the band:

$$z_{cent} = C_1 - C_2 \frac{\theta^{A_1}}{A_2} \exp\left[-\frac{\theta}{B_2}\right] \tag{C.1}$$

where C_1, C_2, A_1, A_2, B_2 are constants. The polar coordinate θ varies $\theta_{max} \geq \theta \geq 0$, where θ_{max} corresponds to the start of the band at the pulmonary aorta, and $\theta = 0$ corresponds to the end of the ascending segment.

The r-coordinate of the centerline should now be constructed in such a way that the centerline correctly skirts the ventricular chamber surfaces. So for a parabolic chamber the centerline r_{cent}:

$$\begin{aligned} r_{cent} &= \sqrt{\frac{1}{A_3} z_{cent} + ZA * C_3}\,[\text{Factor 1}]\,[\text{Factor 2}]\,, \\ \text{Factor 1} &= 1 + C_4 \cos\left(\frac{\theta - \theta_{crossing}}{2}\right), \\ \text{Factor 2} &= 1 + C_5 \exp\left(-\left(\theta - \theta_{right}\right)^2\right), \end{aligned} \tag{C.2}$$

where, A_3, ZA, C_3, C_4 and C_5 are constants. We introduce Factor 1 to avoid self-overlap of the band at $\theta_{\text{crossing}} = \pi\left(-1 + \cot\frac{\pi}{A_1 B_2}\right)$ and $\theta_{\text{crossing}} + 2\pi$. The factor bends the centerline away from self-crossing. We also introduce Factor 2, which is only significant in the region of anterior surface and describes the fact that this surface bends significantly outwards from the septum. We choose the middle of anterior surface to correspond to $\theta_{\text{right}} = 3.8\pi$. The position of the apex of

the left ventricular chamber is taken to be at $z = C_3$. The constants of equations C.1 and C.2 are not independent when related to the geometry of the heart, for example a combined change in A_1 and ZA controls the fiber orientation in the region of the apex. The shape of the chamber can be controlled by changes in the constant A_3. The centerline can also be written in a similar way for a spherical chamber:

$$r_{cent} = \sqrt{\frac{1}{A_3} z_{cent} + ZA * C_3}\,[\text{Factor 1}]\,[\text{Factor 2}] \tag{C.3}$$

where R_0 characterizes the spherical shape of the ventricle, while all the other constants are the same as for equation C.2.

To make the mathematical description of the 3D shape of the band simpler, we approximate the direction of the width to be along the z-axis. The parameterized three dimensional structure is then described in cartesian coordinate, (x, y, z), by:

$$\begin{aligned} z &= z_{cent} + \xi & r &= r_{cent}(z) + \zeta \\ x &= r\cos\theta & y &= r\sin\theta \end{aligned} \tag{C.4}$$

where $-w/2 < \xi < w/2$ and $0 < \zeta < t$, with w and t are the width and the thickness of the band, respectively.

The parameters that remain constant for all models have values of $C_1 = 4.9,\ C_2 = 7,\ A_2 = 0.5,\ C_3 = -0.77,\ C_4 = 1/6$ and $C_5 = 1$. The following is the list of the models used in this paper and the parameter values for each one (unless otherwise specified equation C.2 was used):

Normal: $A_1 = 1.3, ZA = 1.1, A_3 = 1$.

Weakly Oblique: $A_1 = 1.1, ZA = 1.4, A_3 = 1$.

Moderately Oblique: $A_1 = 1.0, ZA = 1.6, A_3 = 1$.

Strongly Oblique: $A_1 = 0.9, ZA = 1.7, A_3 = 1$.

Moderately Dilated: $A_1 = 1.3, ZA = 1.1, A_3 = 1/4$.

Strongly Dilated: In this case equation (C.3) was used with $A_1 = 1.3, ZA = 1.1, A_3 = 1, R_0 = 3.8$.

Other Damage: $A_1 = 1.3, ZA = 1.1, A_3 = 1$.

C.2 Calculating Twist of the Left ventricle

In order to measure twist we attach a strip of soft material to the left ventricle. This strip of material (twist indicator) is made of a material that is two orders of magnitude softer than the non-active

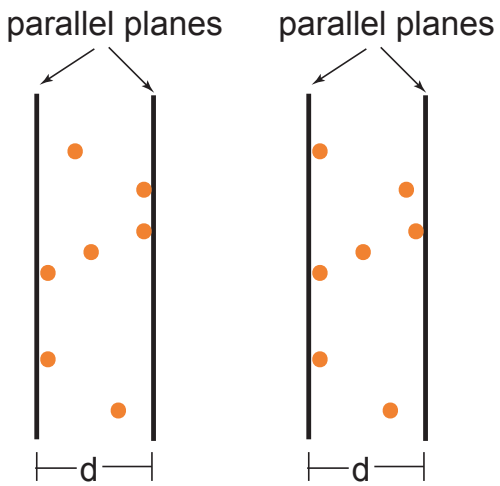

Figure C.1: A sketch of the two dimensional projection of the "sandwich" with markers. Left: a case with two markers on each plane. Right: a case with three markers on one plane and only one marker on the other plane.

material (i.e., the Young's modulus of the twist indicator material is one hundredth of the Young's modulus of the non-active material). As a result the twist indicator does not influence the movement of the band. In its initial configuration the strip is on a vertical plane containing the long axis of the left ventricle and at $\theta = 2.96\pi$. During the deformation of the band the strip can deform in plane or out of the plane. When the long axis of the left ventricle shortens during contraction the indicator strip deforms in plane. In the shortening of the long-axis the top and bottom portions of the left ventricle band come closer together, and to accommodate this deformation the strip buckles outward. However, unless the top and bottom portions of the band rotate with respect to each other, the buckling will occur in the same vertical plane. Conversely, in twisting of the left ventricle the bottom and top portions of the band move with respect to each other in the horizontal plane. As a result the strip deforms out-of-plane. The greater the twist of the left ventricle, the greater the out-of-plane deformation. To measure the out-of-plane deformation we keep track of the position of the nodes on the strip indicator. The way we calculate the out-of-plane distance is akin to the least squares method in 3D, we imagine two parallel planes sandwiching these nodes and minimize the distance between the planes. Because the two planes are always parallel (i.e., the normals are the same) there are two possible arrangements: In the first configuration, one plane is defined by a triplet of points, while the other is defined by a single point and the the normal of the first plane. In the second possible configuration, each plane contains a pair of points (figure C.1). Once the minimum distance, the minimal sandwich thickness, is calculated we can translate that measure directly into twist or torsion. Twist of the left ventricle is normally defined as the slope of the fit line to the relationship between the rotational angle of a marker and its long-axial position. Torsion

of the left ventricle is defined as the average of the rotations of markers placed at different positions of the long-axis. We could use the nodes of the twist indicator as markers and calculate the rotation of each one and then average to calculate torsion or twist, but this would only introduce unnecessary errors. Instead, we directly relate the out-of-plane deformation of the twist indicator to the values of twist and torsion. Assuming that the twist changes linearly with the z-coordinate of the long axis, with no twist at the basal plane and maximal twist at the apex, the maximum out-of-plane movement will be at $\frac{1}{3}$LA from the apex in the case of a parabolic and $(1 - 1/\sqrt{2})R_0$ in the case of a spherical chamber, where LA and R_0 is the long axis and the sphere radius, respectively. As a result twist is calculated from out-of-plane deformation (d) of the twist indicator:

$$\text{twist}_{\text{parabolic}} = -\frac{3\sqrt{3}}{2}\frac{d}{(\text{LA})(\text{r}_{\text{base}})}, \tag{C.5}$$

$$\text{twist}_{\text{sphere}} = -\frac{2d}{R_0^2}, \tag{C.6}$$

where, LA and r_{base} are the long axis length and radius at the base (top), respectively. Once twist is known torsion can be calculated from the relationship between twist and torsion torsion = (LA)twist/2:

$$\text{torsion}_{\text{parabolic}} = \frac{3\sqrt{3}}{4}\frac{d}{r_{base}}, \tag{C.7}$$

$$\text{torsion}_{\text{sphere}} = \frac{d}{R_0}. \tag{C.8}$$

C.3 Calculating radius of curvature

Let $\vec{r}(s)$ be the parametric equation for the curve of interest, where s is the natural parameter. The tangent is given by:

$$\hat{t}(s) = \dot{\vec{r}}(s). \tag{C.9}$$

We know that the relationship between the tangent and the normal can be expressed as:

$$\dot{\hat{t}}(s) = æ \cdot \hat{n}(s), \tag{C.10}$$

where æ is the curvature. The radius of curvature is then given by

$$R = \frac{1}{æ} = \frac{1}{\left\|\dot{\hat{t}}\,(s)\right\|}. \tag{C.11}$$

C.4 Radius of Curvature for a helix about a cylinder

For a helix about a cylinder of radius r where the curve makes γ angle with the vertical, z-coordinate. The parametric equation in terms of natural parameter s is:

$$z = s \cdot \cos\gamma, \qquad \theta = \frac{s}{r}\sin\gamma, \tag{C.12}$$

$$\vec{r}(s) = [x, y, z] = \left[r\cos\left(\frac{s}{r}\sin\gamma\right), r\sin\left(\frac{s}{r}\sin\gamma\right), s\cdot\cos\gamma\right]. \tag{C.13}$$

The tangent is then given by:

$$\hat{t}(s) = \left[-\sin\gamma\sin\left(\frac{s}{r}\sin\gamma\right), \sin\gamma\cos\left(\frac{s}{r}\sin\gamma\right), \cos\gamma\right]. \tag{C.14}$$

The derivative of the tangent is:

$$\dot{\hat{t}}\,(s) = \left[-\frac{1}{r}\sin^2\gamma\cos\left(\frac{s}{r}\sin\gamma\right), -\frac{1}{r}\sin^2\gamma\sin\left(\frac{s}{r}\sin\gamma\right), 0\right]. \tag{C.15}$$

The curvature is then:

$$æ = \left\|\dot{\hat{t}}\,(s)\right\| = \frac{\sin^2\gamma}{r}. \tag{C.16}$$

The radius of curvature is then:

$$R = \frac{r}{\sin^2\gamma}. \tag{C.17}$$

Appendix D

Extra Figures

D.1 Additional figures for chapter 2

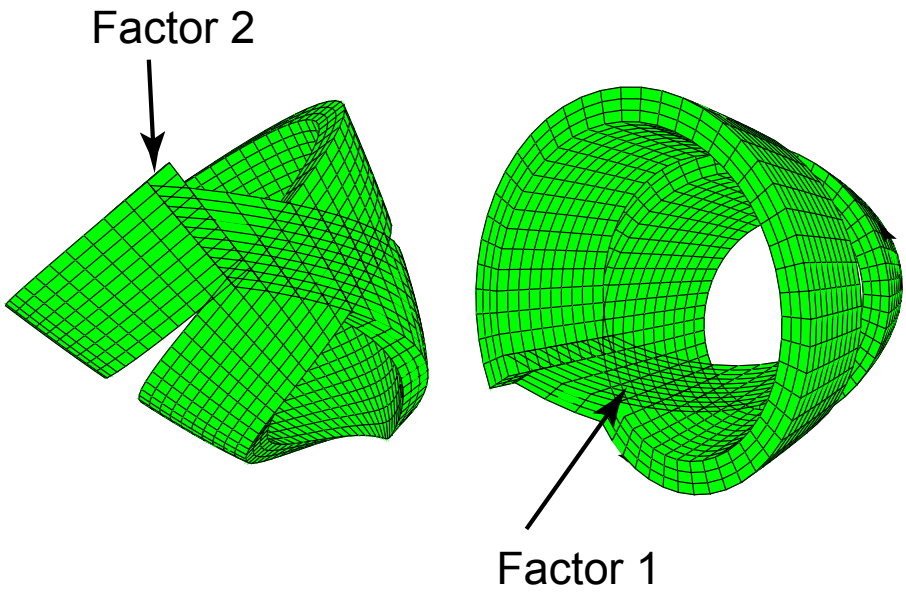

Figure D.1: The form of the band before Factor 1 and Factor 2 were included into equation 2.5. On the left the point at which Factor 2 pulls the band out is indicated. On the right the cross over point which Factor 1 separates is indicated.

D.2 Additional figures for chapter 4

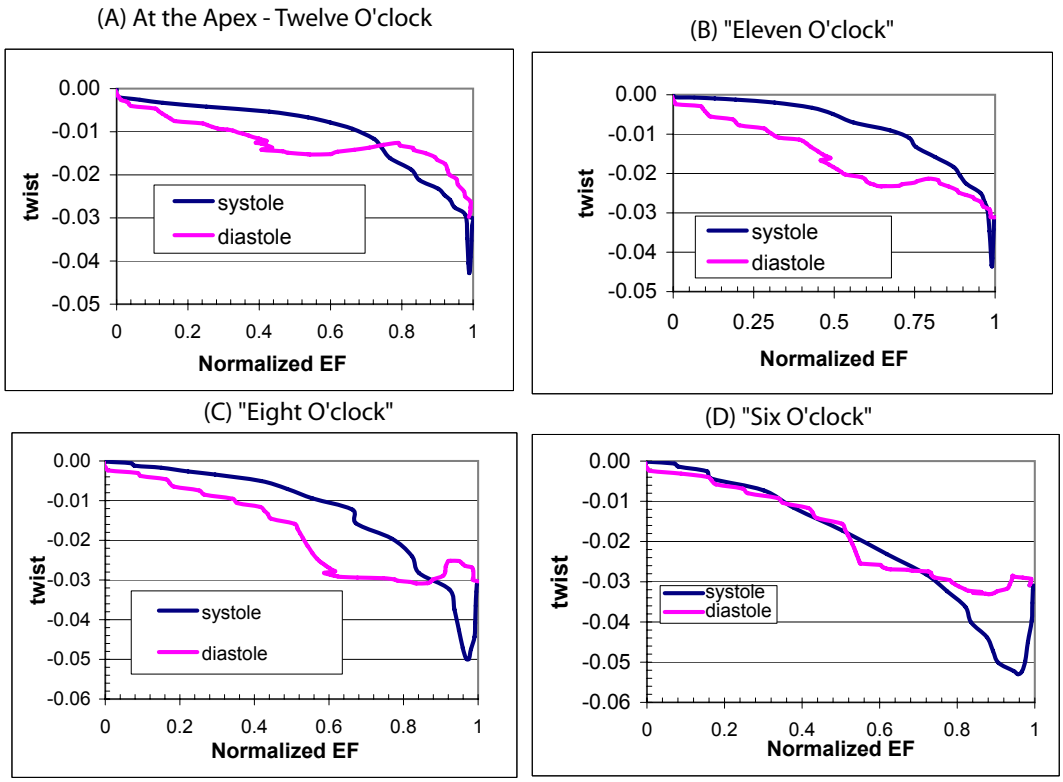

Figure D.2: Twist vs. normalized ejection fraction for spatial waves with varying origin of excitation. (A) The "Purkinje" type wave used through out this dissertation; (B) the wave origin is shifted slightly into the septum; (C) the wave origin is shifted toward the right heart; (D) the wave origin is shifted further towards the right heart. It is interesting to not that the loops seem to collapse forecasting that when the wave originates at the right heart the directions of contractions are reversed.

D.3 Alternate figures for chapter 5

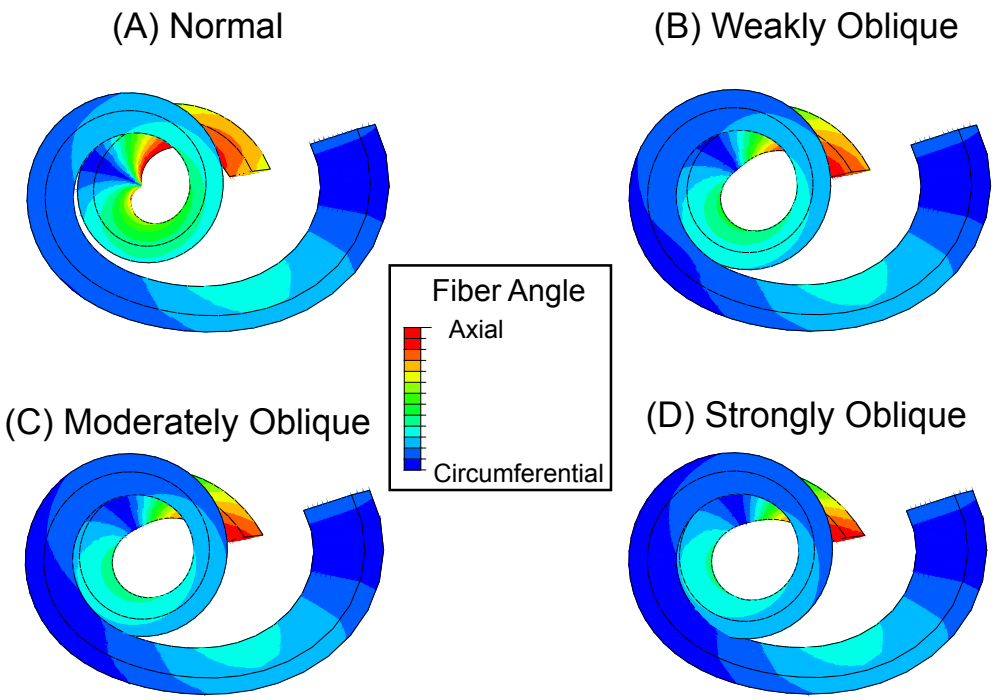

Figure D.3: Top view: The model double helical band is color coded for the fiber angle - blue and red representing circumferential and axial fibers, respectively. The fiber angle was calculated in the same way as in paper by Helm et.al. [23]. (A)"Normal" model with fiber orientation corresponding to physiological. (B)"Weakly Oblique" model showing the fibers close to the apex to be a little more oblique than in the "Normal" case. (C) "Moderately Oblique" model with fibers considerably more oblique in the apical region than would be normal. (D) "Strongly Oblique" model showing the fibers close to the apex region to be almost circumferential.

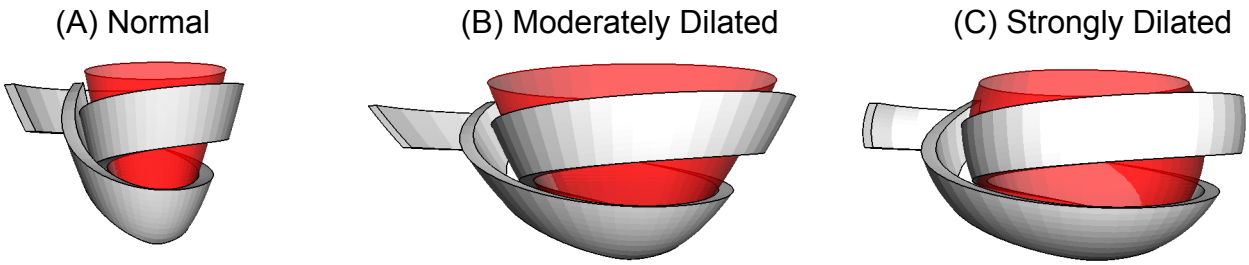

Figure D.4: Different view: The model double helical band (grey) with the fitted left ventricular (LV) volume (red). The long axis dimension in each case is 7 cm. (A)"Normal" model, the LV is approximated with a paraboloid, with the basal radius of ≈ 3.5 cm; (B)"Moderately Dilated" model, the LV is approximated with a paraboloid, with the basal radius of ≈ 6 cm; (C)"Strongly Dilated" model, the LV is approximated with a section of a sphere, with the basal radius of ≈ 7 cm.

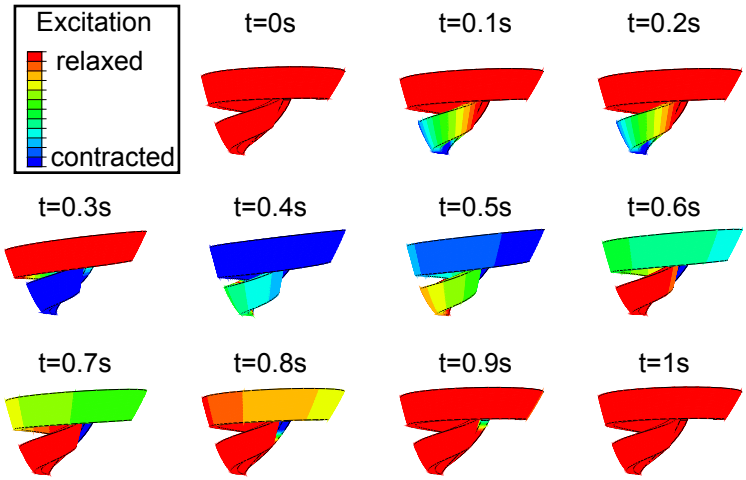

Figure D.5: Side view of the double helical band model color coded for excitation: red and blue correspond to relaxed and excited, respectively. The material is fully contracted (up to 15% shortening) when it is fully excited (blue). The excitation wave starts at the apex and propagates outwards. The band is completely contracted (end-systole) at $t = 0.38s$. During diastole the relaxation wave front also starts from the apex and travels outward.

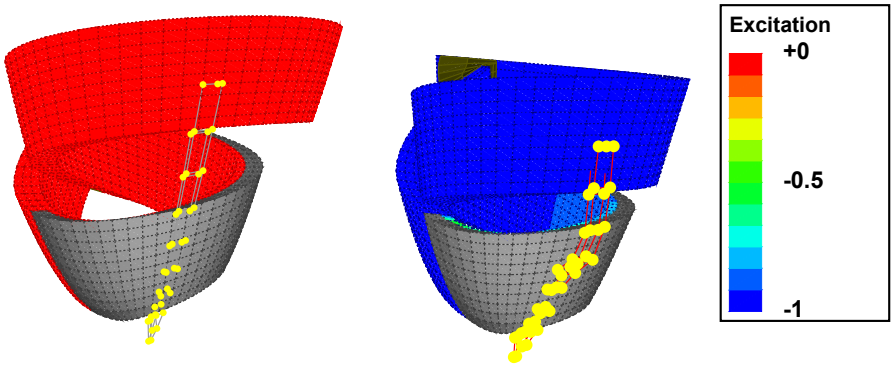

Figure D.6: The double helical band after "infarction" with the twist markers. The band is color coded for excitation: relaxed and fully contracted in red and blue, respectively. The markers are yellow circles connected with grey lines. Grey indicates the dead muscle. The left panel shows the fully relaxed band, with all the markers in plane. The right panel shows the fully contracted band, with the markers our of plane. It is also easy to visually see the volume reduction.

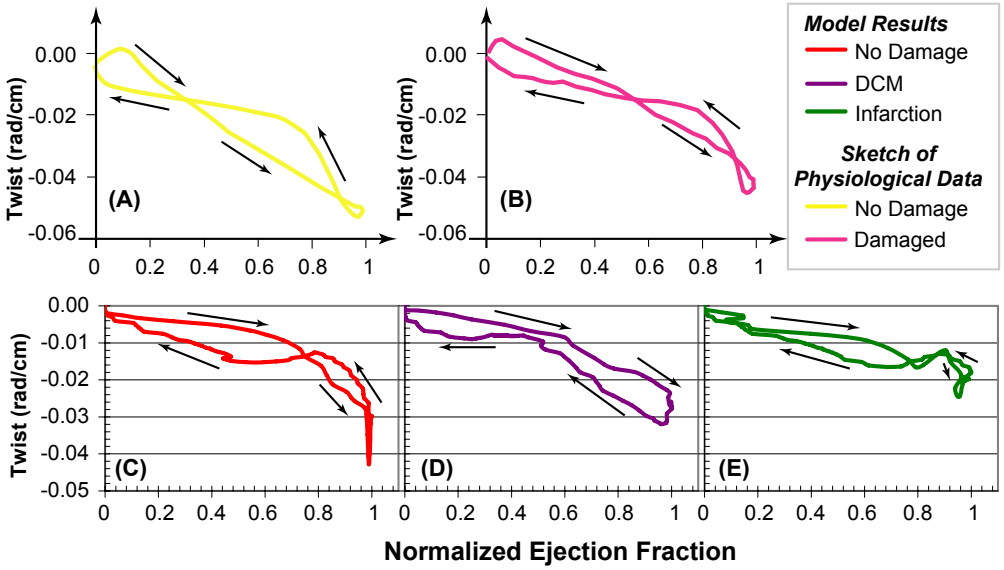

Figure D.7: Twist vs. normalized ejection fraction for: (A) A schematic showing the physiological twist for a normal heart [27]; (B) a compiled schematic for a damaged heart [27, 28];(C) the undamaged model; (D) model of a heart with DCM; (E) Model of the heart after an infarction.

Bibliography

[1] Wayne Rosamond, Katherine Flegal, Gary Friday, Karen Furie, Alan Go, Kurt Greenlund, Nancy Haase, Michael Ho, Virginia Howard, Bret Kissela, Steven Kittner, Donald Lloyd-Jones, Mary McDermott, James Meigs, Claudia Moy, Graham Nichol, Christopher J. O'Donnell, Veronique Roger, John Rumsfeld, Paul Sorlie, Julia Steinberger, Thomas Thom, Sylvia Wasserthiel-Smoller, Yuling Hong, for the American Heart Association Statistics Committee, and Subcommittee Stroke Statistics. Heart disease and stroke statistics–2007 update: A report from the american heart association statistics committee and stroke statistics subcommittee. *Circulation*, 115(5):e69–171, 2007.

[2] Sharon Ann Hunt, William T. Abraham, Marshall H. Chin, Arthur M. Feldman, Gary S. Francis, Theodore G. Ganiats, Mariell Jessup, Marvin A. Konstam, Donna M. Mancini, Keith Michl, John A. Oates, Peter S. Rahko, Marc A. Silver, Lynne Warner Stevenson, Clyde W. Yancy, Elliott M. Antman, Sidney C. Jr. Smith, Cynthia D. Adams, Jeffrey L. Anderson, David P. Faxon, Valentin Fuster, Jonathan L. Halperin, Loren F. Hiratzka, Sharon Ann Hunt, Alice K. Jacobs, Rick Nishimura, Joseph P. Ornato, Richard L. Page, and Barbara Riegel. Acc/aha 2005 guideline update for the diagnosis and management of chronic heart failure in the adult–summary article: A report of the american college of cardiology/american heart association task force on practice guidelines (writing committee to update the 2001 guidelines for the evaluation and management of heart failure): Developed in collaboration with the american college of chest physicians and the international society for heart and lung transplantation: Endorsed by the heart rhythm society. *Circulation*, 112(12):1825–1852, 2005.

[3] Khawaja Afzal Ammar, Steven J. Jacobsen, Douglas W. Mahoney, Jan A. Kors, Margaret M. Redfield, John C. Jr. Burnett, and Richard J. Rodeheffer. Prevalence and prognostic significance of heart failure stages: Application of the american college of cardiology/american heart association heart failure staging criteria in the community. *Circulation*, 115(12):1563–1570, 2007.

[4] William J. Larsen. Development of the heart. In *Human Embryology*, pages 131–155. W. B. Saunders Company, 2nd edition, 1997.

[5] Arian S. Forouhar, Michael Liebling, Anna Hickerson, Abbas Nasiraei-Moghaddam, Huai-Jen Tsai, Jay R. Hove, Scott E. Fraser, Mary E. Dickinson, and Morteza Gharib. The embryonic vertebrate heart tube is a dynamic suction pump. *Science*, 312(5774):751–753, 2006.

[6] Michael Liebling, Arian S. Forouhar, Ralf Wolleschensky, Bernhard Zimmermann, Richard Ankerhold, Scott E. Fraser, Morteza Gharib, and Mary E. Dickinson. Rapid three-dimensional imaging and analysis of the beating embryonic heart reveals functional changes during development. *Developmental Dynamics*, 235(11):2940–2948, 2006. 10.1002/dvdy.20926.

[7] A. N. Moghaddam. *Measurement and Analysis of Structure and Function of Myocardium in Embryonic and Adult Heart*. PhD thesis, California Institute of Technology, 2006.

[8] Abbas Nasiraei-Moghaddam, Michael Liebling, Arian S. Forouhar, Huai-Jen Tsai, Scott E. Fraser, and Morteza Gharib. A lagrangian approach reveals the active and passive regions in the embryonic zebrafish heart. *Annals of Biomedical Engineering*, submitted 2007.

[9] J. B. Cowey. The structure and function of basement membrane muscle system in amphiporus lactifloreus (nemertea). *Quarterly Journal of Microscopical Science*, 93(1):1–15, 1952.

[10] R. B. Clark and J. B. Cowey. Factors controlling the change of shape of certain nemertean and turbellarian worms. *Journal of Experimental Biology*, 35:731–748, 1958.

[11] Thomas Bartman and Jay Hove. Mechanics and function in heart morphogenesis. *Developmental Dynamics*, 233:373–381, 2005.

[12] Jorg Manner. On rotation, torsion, lateralization, and handedness of the embryonic heart loop: New insights from a simulation model for the heart loop of chick embryos. *The Anatomical Record Part A: Discoveries in Molecular, Cellular, and Evolutionary Biology*, 278A(1):481–492, 2004.

[13] D. H. Van Campen, J. M. Huyghe, P. H. M. Bovendeerd, and T. Arts. Biomechanics of the heart muscle. *European Journal of Mechanics, A/Solid*, 13(4-suppl.):19–41, 1994.

[14] Keith L. Moore and Arthur F. Dalley. *Clinically Oriented Anatomy*. Lippincott Williams and Wilkins, New York, 5th edition, 2006.

[15] Arthur C. Guyton and John E. Hall. *Textbook of Medical Physiology*. W.B. Saunders company, New Yourk, 10th edition, 2000.

[16] Jay D. Humphrey. *Cardiovascular Solid Mechanics*. Springer, New York, 2002.

[17] Gerald D. Buckberg. Basic science review: The helix and the heart. *The Journal of Thoracic and Cardiovascular Surgery*, 124(5):863–883, 2002.

[18] L. Krehl. Beitrage zur kenntnis der fullung und entleerung des herzens. *Abh Math-Phys Kl Saechs Akad Wiss*, 17:341–362, 1891.

[19] P.S. Jouk, Yves Usson, Gabrielle Michalowicz, and Laurence Grossi. Three-dimensional cartography of the pattern of the myofibres in the second trimester fetal human heart. *Anatomy and Embryology*, 202(2):103–118, 2000.

[20] Daniel D. Streeter Jr., Henry M. Spotnitz, Dali P. Patel, John Ross, and Edmund H. Sonnenblick. Fiber orientation in the canine left ventricle during diastole and systole. *Circulation Research*, 24:339–347, 1969.

[21] F. Torrent-Guasp, M. J. Kocica, A. F. Corno, M. Komeda, F. Carreras-Costa, A. Flotats, J. Cosin-Aguillar, and H. Wen. Towards new understanding of the heart structure and function. *European Journal of Cardio-Thoracic Surgery*, 27(2):191–201, 2005.

[22] Leonid Zhukov and Alan H. Barr. Heart-muscle fiber reconstruction from diffusion tensor MRI, 2003.

[23] Patrick Helm, Mirza Faisal Beg, Michael I. Miller, and Raimond L. Winslow. Measuring and mapping cardiac fiber and laminar architecture using diffusion tensor MR imaging. *Ann NY Acad Sci*, 1047(1):296–307, 2005.

[24] Francesc Carreras, Manel Ballester, Sandra Pujadas, Ruben Leta, and Guillem Pons-Llado. Morphological and functional evidences of the helical heart from non-invasive cardiac imaging. *Eur J Cardiothorac Surg*, 29(Suppl1):S50–55, 2006.

[25] Joseph C. Walker, Julius M. Guccione, Yi Jiang, Peng Zhang, Arthur W. Wallace, Edward W. Hsu, and Mark B. Ratcliffe. Helical myofiber orientation after myocardial infarction and left ventricular surgical restoration in sheep. *J Thorac Cardiovasc Surg*, 129(2):382–390, 2005.

[26] Neil B. Ingels Jr. Myocardial fiber architecture and left ventricular function. *Technology and Health Care*, 5:45–52, 1997.

[27] Marc R. Moon, Neil B. Ingels Jr., George T. Daughters II, Edward B. Stinson, David E. Hanses, and D. Craig Miller. Alterations in left ventricular twist mechanics with inotropic stimulation and volume loading in human subjects. *Circulation*, 89(1):142–150, 1994.

[28] Kwok L. Yun, Marek A. Niczyporuk, George T. Daughters II, Neil B. Ingels Jr., Edward B. Stinson, Edwin L. Alderman, David E. Hanses, and D. Craig Miller. Alterations in left ventircular diastolic twist mechanics during acute human cardiac allograft rejection. *Circulation*, 83 (3):962–973, 1991.

[29] R. Beyar, F. C. P. Yin, M. Hausknecht, M. L. Weisfeldt, and D. A. Kass. Dependence of left-ventricular twist-radial shortening relations on cardiac cycle phase. *American Journal of Physiology*, 257(4):H1119–H1126, 1989. Part 2.

[30] M. Takeuchi, T. Nishikage, H. Nakai, M. Kokumai, S. Otani, and R. M. Lang. The assessment of left ventricular twist in anterior wall myocardial infarction using two-dimensional speckle tracking imaging. *Journal of the American Society of Echocardiography*, 20(1):36–44, 2007.

[31] M. Stuber, M. B. Scheidegger, S. E. Fischer, E. Nagel, F. Steinemann, O. M. Hess, and P. Boesiger. Alterations in the local myocardial motion pattern in patients suffering from pressure overload due to aortic stenosis. *Circulation*, 100(4):361–368, 1999.

[32] E. Nagel, M. Stuber, B. Burkhard, S. E. Fischer, M. B. Scheidegger, P. Boesiger, and O. M. Hess. Cardiac rotation and relaxation in patients with aortic valve stenosis. *Eur Heart J*, 21 (7):582–589, 2000.

[33] M. Takeuchi, H. Nakai, M. Kokumai, T. Nishikage, S. Otani, and R. M. Lang. Age-related changes in left ventricular twist assessed by two-dimensional speckle-tracking imaging. *Journal of the American Society of Echocardiography*, 19(9):1077–1084, 2006.

[34] F. E. Rademakers, M. B. Buchalter, W. J. Rogers, E. A. Zerhouni, M. L. Weisfeldt, J. L. Weiss, and E. P. Shapiro. Dissociation between left ventricular untwisting and filling. accentuation by catecholamines. *Circulation*, 85(4):1572–1581, 1992.

[35] Larry A. Taber, Ming Yang, and W. William Podszus. Mechanics of ventricular torsion. *Journal of Biomechanics*, 29(6):742–752, 1996.

[36] D. P. Zipes, P. Libby, R. O. Bonow, and E. Braunwald. *Braunwald's Heart Disease: A Textbook of Cardiovascular Medicine*. W. B. Saunders, St. Louis, MO, 7th edition, 2005.

[37] Constantine L. Athanasuleas, Alfred W. H. Stanley, Gerald D. Buckberg, Vincent Dor, Marissa DiDonato, and Eugene H. Blackstone. Surgical anterior ventricular endocardial restoration (saver) in the dilated remodeled ventricle after anterior myocardial infarction. *Journal of the American College of Cardiology*, 37(5):1199–1209, 2001.

[38] A. P. Furnary, F. M. Jessup, and L. P. Moreira. Multicenter trial of dynamic cardiomyoplasty for chronic heart failure. (the american cardiomyoplasty group.). *J Am Coll Cardiol*, 28(5): 1175–1180, 1996.

[39] M. A. Pfeffer and E. Braunwald. Ventricular remodeling after myocardial infarction. experimental observations and clinical implications. *Circulation*, 81(4):1161–1172, 1990.

[40] H. M. Hurlburt, G. P. Aurigemma, J. C. Hill, A. Narayanan, W. H. Gaasch, C. S. Vinch, T. E. Meyer, and D. A. Tighe. Direct ultrasound measurement of longitudinal, circumferential, and radial strain using 2-dimensional strain imaging in normal adults. *Echocardiography – a Journal of Cardiovascular Ultrasound and Allied Techniques*, 24(7):723–731, 2007.

[41] Edward A. Sallin. Fiber orientation and ejection fraction in the human left ventricle. *Biophysics Journal*, 9(7):954–64, 1969.

[42] Charles S. Peskin and David M. McQueen. A general method for the computer simulation of biological systems interacting with fluids. *Sym Soc Exp Biol.*, 49:265–76, 1995.

[43] Sandor J. Kovacs, David M. McQueen, and Charles S. Peskin. Modelling cardiac fluid dynamics and diastolic function. *Philosophical Transactions of the Royal Society A: Mathematical, Physical and Engineering Sciences*, 359(1783):1299 – 1314, 2001.

[44] Peter J. Hunter, Andrew J. Pullan, and Bruce H. Smaill. Modeling total heart function. *Annu Rev Biomed Eng*, 5:147–77, 2003.

[45] Marko Vendelin, Peter Bovendeerd, Juri Engelbrecht, and Theo Arts. Optimizing ventricular fibers: Uniform strain or stress, but not atp consumption, leads to high efficiency. *American Journal of Physiology*, 283:1072–1081, 2002.

[46] Hiroshi Watanabe, Toshiaki Hisada, Seiryo Sugiura, Jun-ichi Okada, and Hiroshi Fukunari. Computer simulation of blood flow, left ventricular wall motion and their interrelationship by fluid-structure interaction finite element method. *JSME International Journal Series C Mechanical Systems, Machine Elements and Manufacturing*, 45(4):1003–1012, 2002.

[47] A.D. McCulloch and R. Mazhari. Regional myocardial mechanics: Integrative computational models of flow-function relations. *J Nucl Cardiol.*, 8(4):506–19, 2001.

[48] A. D. McCulloch. Functionally and structurally integrated computational modeling of ventricular physiology. *Japanese Journal of Physiology*, 54(6):531–539, 2004.

[49] Kevin D. Costa, Yasuo Takayama, Andrew D. McCulloch, and James W. Covell. Laminar fiber architecture and three-dimensional systolic mechanics in canine ventricular myocardium. *Am J Physiol Heart Circ Physiol*, 276(2):H595–607, 1999.

[50] John C. Criscione, Andrew D. McCulloch, and William C. Hunter. Constitutive framework optimized for myocardium and other high-strain, laminar materials with one fiber family. *Journal of the Mechanics and Physics of Solids*, 50:1681–1702, 2002.

[51] K.d. Costa, P. J. Hunter, J.M. Rogers, Julius M. Guccione, L.K. Waldman, and Andrew D. McCulloch. A three-dimensional finite element method for large ventricular myocardium. *Transactions of the ASME*, 118:452–72, 1996.

[52] Roy C. P. Kerckhoffs, Maxwell L. Neal, Quan Gu, James B. Bassingthwaighte, Jeff H. Omens, and Andrew D. McCulloch. Coupling of a 3d finite element model of cardiac ventricular mechanics to lumped systems models of the systemic and pulmonic circulation. *Annals of Biomedical Engineering*, 35(1):1–18, 2007.

[53] T. P. Usyk and A. D. McCulloch. Electromechanical model of cardiac resynchronization in the dilated failing heart with left bundle branch block. *Journal of Electrocardiology*, 36:57–61, 2003.

[54] T. P. Usyk, I. J. LeGrice, and A. D. McCulloch. Computational model of three-dimensional cardiac electromechanics. *Computing and Visualization in Science*, 4(4):249–257, 2002.

[55] Partho P. Sengupta, Josef Korinek, Marek Belohlavek, Jagat Narula, Mani A. Vannan, Arshad Jahangir, and Bijoy K. Khandheria. Left ventricular structure and function, basic science for cardiac imaging. *Journal of the American College of Cardiology*, 48(10):1988–2001, 2006.

[56] Partho P. Sengupta, Vijay K. Krishnamoorthy, Josef Korinek, Jagat Narula, Mani A. Vannan, Steven J. Lester, Jamil A. Tajik, James B. Seward, Bijoy K. Khandheria, and Marek Belohlavek. Left ventricular form and function revisited: Applied translational science to cardiovascular ultrasound imaging. *Journal of the American Society of Echocardiography: Official publication of the American Society of Echocardiography*, 20(5):539–551, 2007.

[57] James C. O'Reilly, Dale A. Ritter, and David R. Carrier. Hydrostatic locomotion in a limbless tetrapod. *Nature*, 386(6622):269–272, 1997.

[58] B. A Dubrovin, A. T Fomenko, and S. P. Novikov. *Modern Geometry–Methods and Applications*. Springer series in Soviet mathematics, Graduate texts in mathematics. Springer-Verlag, New York, 2nd edition, 1992.

[59] Gerald D. Buckberg, Myron L. Weisfeldt, Manel Ballester, Raphael Beyar, Daniel Burkhoff, H. Cecil Coghlan, Mark Doyle, Neal D. Epstein, Morteza Gharib, Ray E. Ideker, Neil B. Ingels, Martin M. LeWinter, Andrew D. McCulloch, Gerald M. Pohost, Leslie J. Reinlib, David J. Sahn, George Sopko, Francis G. Spinale, Henry M. Spotnitz, Francisco Torrent-Guasp, and Edward P. Shapiro. Left ventricular form and function: Scientific priorities and strategic planning for development of new views of disease. *Circulation*, 110(14):e333–336, 2004.

[60] Richard P. Harvey and Nadia Rosenthal. *Heart Development*. Academic Press, San Diego, CA, 1999.

[61] Claus Mattheck. *Design in Nature: Learning from Trees*. Springer, New York, 1998.

[62] H.R. Crane. Principles and problems of biological growth. *The Scientific Monthly*, 70(6): 376–389, 1950.

[63] Martin Kemp. Spirals of life: D'arcy thompson and theodore cook, with leonardo and durer in retrospect. *Physis; rivista internazionale di storia della scienza*, 32(1):37–54, 1995.

[64] D. E. Hansen, G. T. d Daughters, E. L. Alderman, N. B. Ingels, E. B. Stinson, and D. C. Miller. Effect of volume loading, pressure loading, and inotropic stimulation on left ventricular torsion in humans. *Circulation*, 83(4):1315–1326, 1991.

[65] A. Needleman, S. A. Rabinowitz, D. K. Bogen, and T. A. McMahon. A finite-element model of the infarcted left-ventricle. *Journal of Biomechanics*, 16(1):45–58, 1983.

[66] K. Sunagawa and K. Sagawa. Models of ventricular contraction based on time-varying elastance. *Crc Critical Reviews in Biomedical Engineering*, 7(3):193–228, 1982.

[67] P. H. M. Bovendeerd, T. Arts, T. Delhaas, J. M. Huyghe, D. H. Vancampen, and R. S. Reneman. Regional wall mechanics in the ischemic left ventricle: Numerical modeling and dog experiments. *American Journal of Physiology-Heart and Circulatory Physiology*, 39(1):H398–H410, 1996.

[68] T. Arts, P. Bovendeerd, T. Delhaas, and F. Prinzen. Modeling the relation between cardiac pump function and myofiber mechanics. *Journal of Biomechanics*, 36(5):731–736, 2003.

[69] T. Arts, T. Delhaas, P. Bovendeerd, X. Verbeek, and F. W. Prinzen. Adaptation to mechanical load determines shape and properties of heart and circulation: the circadapt model. *American Journal of Physiology-Heart and Circulatory Physiology*, 288(4):H1943–H1954, 2005.

[70] Vincent Dor, Marisa Di Donato, Michel Sabatier, Francoise Montiglio, Filippo Civaia, and RESTORE Group. Left vetnricular reconstruction by endoventricular circular patch plasty repair: A 17-year experience. *Seminars in Thoracic and Cardiovascular Surgery*, 13(4):435–447, 2001.

[71] Peng Zhang, Julius M. Guccione, Susan I. Nicholas, Joseph C. Walker, Philip C. Crawford, Amin Shamal, David A. Saloner, Arthur W. Wallace, and Mark B. Ratcliffe. Left ventricular volume and function after endoventricular patch plasty for dyskinetic anteroapical left ventricular aneurysm in sheep. *Journal of Thoracic and Cardiovascular Surgery*, 130(4):1032–1038, 2005.

[72] Hiromi Nakai, Masaaki Takeuchi, Tomoko Nishikage, Michiko Kokumai, Shinichiro Otani, and Roberto M. Lang. Effect of aging on twist-displacement loop by 2-dimensional speckle tracking imaging. *Journal of the American Society of Echocardiography*, 19(7):880–885, 2006.

[73] Frederick A. Tibayan, David T. M. Lai, Tomasz A. Timek, Paul Dagum, David Liang, George T. Daughters, Neil B. Ingels, and D. Craig Miller. Alterations in left ventricular torsion in tachycardia-induced dilated cardiomyopathy. *J Thorac Cardiovasc Surg*, 124(1):43–49, 2002.

[74] Inc ABAQUS. *ABAQUS Version 6.5 commercial computer software documentation*. Hibbitt, Karlsson and Sorensen Inc., Plymouth, MI USA, 2004.

[75] Harm J. Muntinga, Frederik van den Berg, Hans R. Knol, Menco G. Niemeyer, Paul K. Blanksma, Henk Louwes, and Ernst E. van der Wall. Normal values and reproducibility of left ventricular filling parameters by radionuclide angiography. *The International Journal of Cardiac Imaging*, 13(2):165–171, 1997.

[76] Fumio Yuasa, Tsutomu Sumimoto, Toshihiko Hattori, Toshimitsu Jikuhara, Makoto Hikosaka, Tetsuro Sugiura, and Toshiji Iwasaka. Effects of left ventricular peak filling rate on exercise capacity 3 to 6 weeks after acute myocardial infarction. *Chest*, 111(3):590–594, 1997.

[77] D. Ajami, O. Oeckler, A. Simon, and R. Herges. Synthesis of a mobius aromatic hydrocarbon. *Nature*, 426(6968):819–821, 2003.

[78] David M. Lemal. Aromatics do the twist. *Nature*, 426:776–77, 2003.

[79] Piotr Pieranski, Justyna Baranska, and Arne Skjeltorp. Tendril perversion–a physical implication of the topological conservation law. *European Journal of Physics*, 25:613–21, 2004.

[80] Jeremy M. Berg, John L. Tymoczko, and Lubert Stryer. *Biochemestry*. W. H. Freeman and Company, New York, 5th edition, 2002.

[81] Yehuda Snir and Randall D. Kamien. Enropically driven helix formation. *Science*, 307:1067, 2005.

[82] T.A. Cook. *The Curves of Life*. Dover, 1979.